MATERIALS SCIENCE

Brightening deep-blue perovskite light-emitting diodes: A path to Rec. 2020

Seungjae Lee[1]†, Junho Kim[1]†, Hyojun Kim[1], Changwon Kim[2], Siin Kim[2], Changjo Kim[1], Heeseung Lee[1], Bongjun Choi[1], Chinnadurai Muthu[1], Taehyun Kim[1], Jihyung Lee[1], Seungbok Lee[1], Hyotcherl Ihee[2,3], Jung-Yong Lee[1]*

Deep-blue perovskite light-emitting diodes (PeLEDs) of high purity are highly sought after for next-generation displays complying with the Rec. 2020 standard. However, mixed-halide perovskite materials designed for deep-blue emitters are prone to halide vacancies, which readily occur because of the low formation energy of chloride vacancies. This degrades bandgap instability and performance. Here, we propose a chloride vacancy–targeting passivation strategy using sulfonate ligands with different chain lengths. The sulfonate groups have a strong affinity for lead(II) ions, effectively neutralizing vacancies. Our strategy successfully suppressed phase segregation, yielding color-stable deep-blue PeLEDs with an emission peak at 461 nanometers and a maximum luminance (*Lmax*) of 2707 candela per square meter with external quantum efficiency (EQE) of 3.05%, one of the highest for Rec. 2020 standard–compliant deep-blue PeLEDs. We also observed a notable increase in EQE up to 5.68% at *Lmax* of 1978 candela per square meter with an emission peak at 461 nanometers by changing the carbon chain length.

INTRODUCTION

Metal halide perovskites (MHPs) have attracted considerable interest for a wide range of optoelectronic applications, including solar cells, light-emitting diodes (LEDs), photodetectors, and phototransistors. Their appeal stems from their facile optical bandgap tunability and balanced charge transport, which enable the development of highly efficient devices (*1*–*4*). In particular, the emitting light colors of MHPs can be easily controlled by adjusting the ratio of halide anions (*5*, *6*). Moreover, the emission spectra of MHPs have a considerably narrow full width at half maximum (FWHM), allowing a wide color gamut of displays for Rec. 2020 color standard specifications (*7*).

Despite the numerous advantages of MHPs, deep-blue perovskite LEDs (PeLEDs) have proven to be a bottleneck in the realization of high-performance perovskite displays mainly due to their low external quantum efficiencies (EQEs) and limited maximum luminance (L_{max}). The advancement in deep-blue brightness is particularly important for applications such as smartphones, which require a brightness of up to 2000 cd/m^2 to ensure visibility under bright outdoor conditions. Green and red PeLEDs satisfy the Rec. 2020 standard and exhibit excellent EQEs of over 25% and L_{max} ranging from 10,000 to 200,000 cd/m^2 (*8*–*13*). However, the world-record EQE of deep-blue LEDs (wavelength < 465 nm) is ~10%, and their L_{max} values fall below 1000 cd/m^2 (*10*, *14*–*19*). Therefore, further research is necessary to devise deep-blue PeLEDs that meet the Rec. 2020 standard and achieve performance levels comparable to those of red and green PeLEDs (*10*–*13*, *20*, *21*).

Various strategies have been used to fabricate deep-blue PeLEDs. A notable method involves the use of low-dimensional perovskite structures. However, these structures tend to result in insufficient charge injection because of the presence of dielectric ligands. Moreover, the color purity can be affected by the presence of nonuniform phases with different n values (where $n = 1, 2, ...$), which can lead to variations in the spectral characteristics of the emitted light (*22*–*24*). Alternatively, blue MHPs can be fabricated by mixing chloride and bromide anions; deep-blue MHPs require a higher fraction of chloride in the mixture. However, the low formation energy of chloride vacancies induces numerous deeper defect sites within the bandgap (*25*, *26*). These defects prompt nonradiative recombination of injected charge carriers, which negatively affects the performance of deep-blue PeLEDs (*26*–*28*).

In addition, halide vacancies in deep-blue PeLEDs can cause severe phase segregation under an operating bias because the vacancies can provide migration channels for intrinsic halide anions (*29*). The phase segregation generates heterogeneous domains with undesired bandgaps in films and broadens the emission spectra (*10*, *30*). Charge carriers in the heterogeneous films tend to funnel into domains with a smaller bandgap. This migration results in a red shift of the emission spectra and, ultimately, color instability of deep-blue PeLEDs (*24*, *31*). Numerous studies have reported the use of ammonium group–based ligands to passivate uncoordinated halide anions to address the issues arising from halide anions (*23*, *32*–*34*). However, in deep-blue PeLEDs, as the ratio of chloride to halide increases, the probability of forming halide vacancies owing to the weak bonding of Pb—Cl surpasses that of forming uncoordinated halide anion defects (*25*, *26*). This complexity presents a substantial hurdle in effectively passivating defects and enhancing the performance of deep-blue PeLEDs. Unexpectedly, strategies for passivating halide vacancies have received relatively less attention to date (*26*).

In this study, we introduce a novel chloride vacancy–targeting passivation strategy that uses sulfonate ligands with varying chain lengths, including methanesulfonate (MS), ethanesulfonate (ES), and propanesulfonate (PS). Sulfonate functional groups exhibit a strong binding affinity with Pb(II) ions, allowing for effective passivation of halide vacancies (*35*). Using this approach, we developed deep-blue MS-treated perovskite (MSP)–based LED devices,

[1]School of Electrical Engineering (EE), Korea Advanced Institute of Science and Technology (KAIST), 291 Daehak-ro, Yuseong-gu, Daejeon 34141, Republic of Korea. [2]Department of Chemistry, Korea Advanced Institute of Science and Technology (KAIST), 291 Daehak-ro, Yuseong-gu, Daejeon 34141, Republic of Korea. [3]Center for Advanced Reaction Dynamics (CARD), Institute for Basic Science (IBS), Daejeon 34141, Republic of Korea.
*Corresponding author. Email: jungyong.lee@kaist.ac.kr
†These authors contributed equally to this work.

achieving an emission peak at 461 nm, an EQE of 3.05%, and an L_{max} of 2707 cd/m^2 with a narrow FWHM of 15.4 nm. Furthermore, LEDs based on ES-treated perovskite (ESP) and PS-treated perovskite (PSP) exhibited improved EQE of 3.96 and 5.68%, respectively. We achieved one of the highest reported values of L_{max} for deep-blue PeLEDs that satisfy the Rec. 2020 color standard. In particular, strong binding passivation by sulfonate ligands efficiently prevents halide migration under bias in mixed-halide perovskite films containing chloride and bromide. Consequently, our chloride vacancy–targeting passivation strategy greatly enhances color stability, as indicated by the changes in the Commission Internationale de l'Élcairage (CIE) coordinates.

RESULTS

Perovskite thin films with improved bandgap stability using sulfonate ligands

Perovskites with sulfonate ligands can be easily synthesized using a simple one-pot solution method. A one-pot precursor solution was prepared by combining cesium (Cs), lead (Pb), bromine (Br), chlorine (Cl), and sulfonate ligands in a dimethyl sulfoxide (DMSO) solvent, which was then subjected to an elevated temperature of 60°C. Subsequently, a diluted mixture of poly(3,4-ethylenedioxythiophene) polystyrene sulfonate (PEDOT:PSS), perfluorinated ionomer (PFI), and fluorosurfactant (FS) was spin-coated onto an indium tin oxide (ITO)/glass substrate to form a hole injection layer. Next, the one-pot precursor solution was spin-coated onto the hole injection layer, followed by antisolvent treatment and thermal annealing at 90°C to promote crystallization (Fig. 1A). Detailed descriptions of the experimental conditions are provided in the experimental section. The SO_3^- group of sulfonate ligands has a lone pair of electrons, which enable them to form strong chemical bonds with Pb ions. This bonding interaction results in a reduction in the number of halide vacancies, which are known to generate channels for anion hopping (*29*). Reducing the number of vacancies suppresses the formation of these channels, which decreases ion migration within the material. As shown in Fig. 1B, phase segregation induced by ion migration can cause exciton funneling, which may lead to the undesired emission of photons.

Analysis of chemical and structural properties of perovskite with sulfonate ligands

The successful incorporation of sulfonate ligands into the perovskite films was confirmed by conducting x-ray photoelectron spectroscopy (XPS) and Fourier transform infrared (FTIR) spectroscopy analyses on control perovskite (CP), MSP, ESP, and PSP films with the amount of the ligands that showed highest photoluminescence (PL) quantum yield (PLQY) of MSP. The XPS S 2p spectra depicted

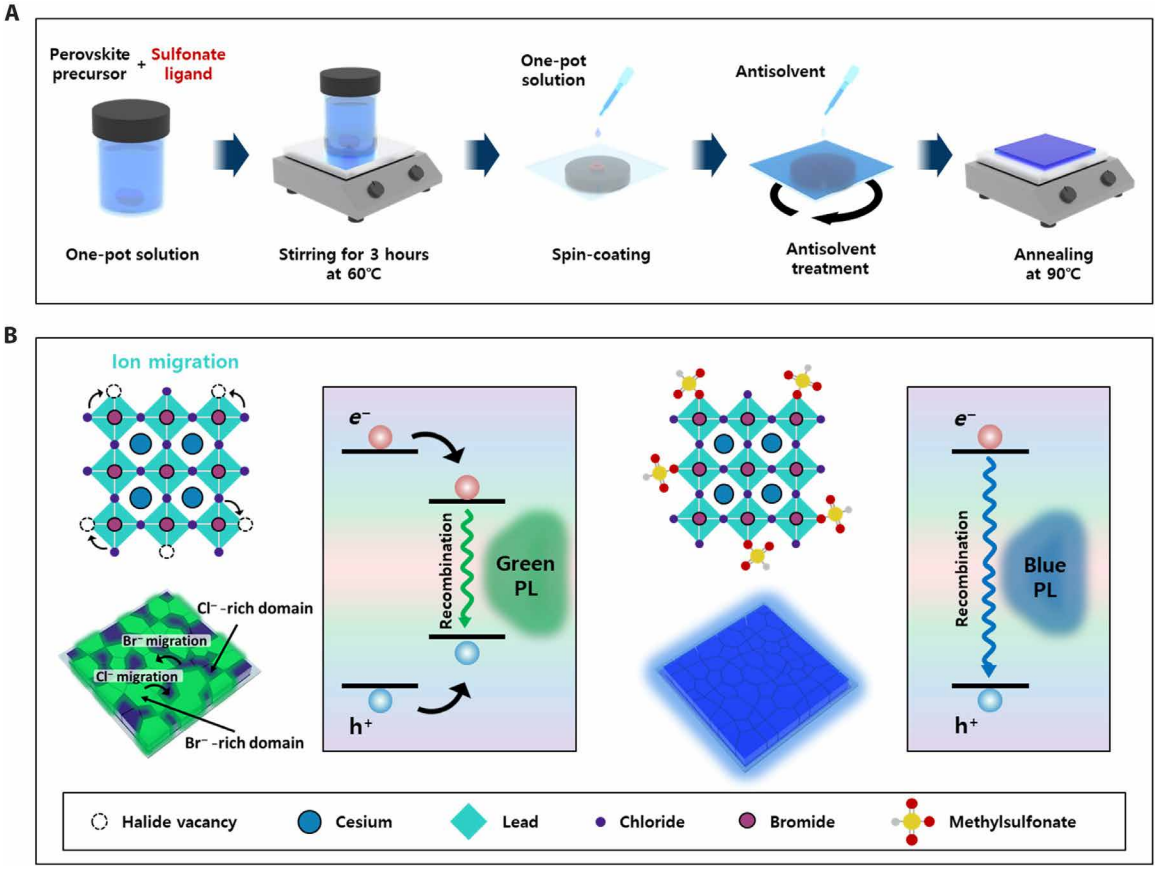

Fig. 1. Procedure and concept of sulfonate ligand–treating perovskite film. (**A**) Schematic of the simple one-pot process for the fabrication of perovskite films incorporating sulfonate ligands. (**B**) Comparative schematics of the control perovskite (CP)–treated perovskite and MSP. CP experiences phase segregation, which leads to exciton funneling and the emission of photons at undesired wavelengths. In contrast, MSP remains free from phase segregation.

in Fig. 2A reveal that no S 2p peaks are detected in the CP film, whereas the MSP film exhibits an S 2p spectrum ranging from 166 to 171 eV. In particular, the S 2p spectrum can be separated into two peaks centered at 167.8 and 169.0 eV, which correspond to SO_3—C and Pb—O—S, respectively (*36*). The appearance of the SO_3—C peak in the MSP films suggests the successful incorporation of sulfonate ligands. Moreover, the occurrence of a Pb—O—S peak provides clear evidence that the sulfonate ligands effectively bonded with the Pb ions, thereby potentially passivating the halide vacancies. Furthermore, the depth profile analysis, as presented in fig. S1, confirmed that sulfonate ligands are distributed throughout the entire perovskite films. We thoroughly examined the high-resolution Pb 4f and Br 3d peaks, spanning the ranges of 135 to 147 eV and 65 to 71 eV, respectively, to validate the chemical bonding between the sulfonate groups and Pb ions. As shown in Fig. 2B, the spectrum of the CP film can be resolved into distinct peaks corresponding to metallic Pb (Pb^0) and Pb ions (Pb^{2+}). The peaks of Pb^0 at 136.2 and 141.1 eV, known as nonradiative recombination sites, reveal insufficient passivation of the CP film (*37*). The Pb^{2+} species in MSP and CP were also analyzed through the Pb $4f^{7/2}$ and Pb $4f^{5/2}$ orbitals. MSP exhibits binding energies at 138.1 and 142.9 eV that are lower than those for CP, which exhibits values of 138.5 and 143.3 eV (dashed lines in Fig. 2B). The lower binding energies can be attributed to the presence of negative charges on the sulfonate groups. These negative charges contribute electron clouds to the Pb ions, filling the Pb 6p orbitals (*38*). This leads to a decrease in the binding energy observed in the MSP spectrum (*38*, *39*). The disappearance of Pb^0 peaks and the peak shifts of Pb $4f^{7/2}$ and Pb $4f^{5/2}$ observed in the MSP also confirm successful bond formation between the Pb ions and sulfonate ligands in the perovskite films. Analysis of the Br 3d spectra, as presented in Fig. 2C, reveals that the MSP exhibits binding energy values of 68.1 and 69.1 eV, lower than those of the CP, at 68.3 and 69.3 eV (dashed lines in Fig. 2C). This can be attributed to the augmentation of electron clouds in the vicinity of Br ions, which arises from the formation of chemical bonds between the Pb ions and sulfonate groups (*40*). Hence, the peak shift observed in the Br 3d spectra offers further proof of the successful incorporation of sulfonate ligands into the perovskite films. XPS analyses of ESP and PSP are shown in fig. S1.

FTIR analysis was conducted to clarify the identity of ligands (Fig. 2D and fig. S2). As shown in Fig. 2D, no peaks are detected within the range of 800 to 1600 cm^{-1} in the CP films. However, the MSP films clearly exhibit peaks related to the alkane bending vibration [ν(C—H)] at 1380 and 1410 cm^{-1} and the S═O stretching vibration [ν(S═O)] at 1050 and 1200 cm^{-1} (*41*).

X-ray diffraction (XRD) was performed to investigate the crystallographic changes induced by the MS, ES, and PS ligands (Fig. 2E and fig. S3). As shown in Fig. 2E, the introduction of sulfonate ligands resulted in the emergence of the (100) plane as the dominant facet. Meanwhile, the (100), (110), (200), (210), (211), and (202) planes of the cubic *Pm*-3*m* structure remained unchanged without the occurrence of additional peaks (*42*–*44*). The (100) plane is recognized for its superior characteristics pertaining to charge transport and low defect density (*45*). The improved charge transport and minimized defect density are essential for achieving high brightness and EQE in LEDs. Therefore, from a crystallographic perspective,

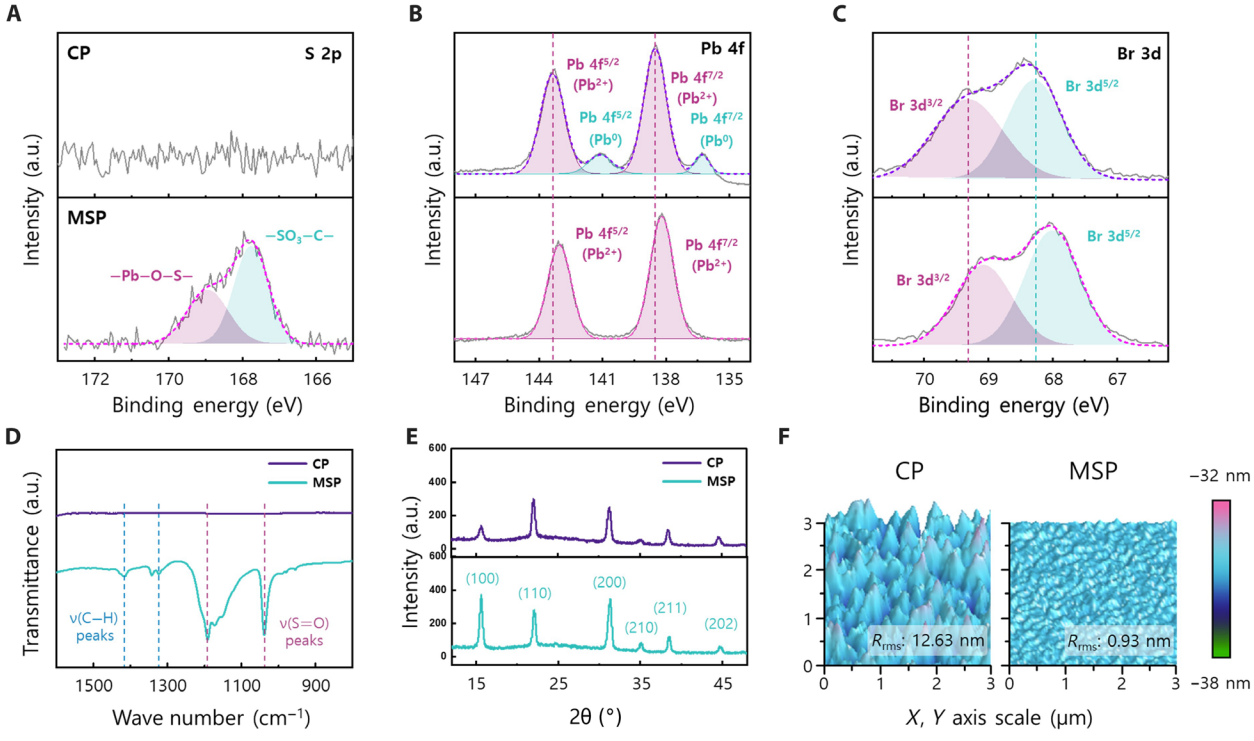

Fig. 2. Comparison between control and sulfonate-treated perovskite. (**A** to **C**) XPS data for different elements in both CP and MSP, including (A) S 2p within the range of 172 to 166 eV, (B) Pb 4f within the range of 147 to 135 eV, and (C) Br 3d within the range of 71 to 66 eV. a.u., arbitrary units. (**D**) FTIR spectra of CP and MSP showing the presence of sulfonate ligands. (**E**) X-ray diffraction (XRD) patterns of CP and MSP, illustrating the crystallographic variations. (**F**) Atomic force microscopy images and roughness of CP and MSP, demonstrating the differences in film quality. rms, root mean square.

sulfonate ligands are promising passivation agents for perovskite materials. Furthermore, the absence of additional peaks indicates that the incorporation of sulfonate ligands did not cause the formation of a two-dimensional (2D) structure (*46*). The lack of a 2D structure is also confirmed by the absence of additional peaks in the ultraviolet-visible absorption spectra (fig. S4) (*47*, *48*). Consequently, the original cubic structure was preserved, which is known for its excellent emission properties (*49*). Detailed analyses of ESP and PSP films are provided in figs. S1 to S3.

Atomic force microscopy scan reveals that the roughness of perovskite film was remarkably reduced from 12.63 to 0.93 nm upon MS incorporation (Fig. 2F). Moreover, scanning electron microscopy images show that the incorporation of MS ligands reduced the grain size from ~300 to 120 nm (fig. S5). This change is due to the suppression of crystal growth during film formation (*50*). The reduction in grain size, driven by the presence of sulfonate ligands, promotes the spatial confinement of charge carriers, leading to enhanced radiative recombination (*51*).

Effect of sulfonate ligands on the photophysical properties

We conducted a comprehensive PL-based analysis to assess the impact of the sulfonate ligands by comparing the properties of CP and MSP. We investigated the temperature-dependent PL ranging from 83 to 243 K for both CP and MSP (Fig. 3, A and B). The integrated PL intensity was applied to the following modified Arrhenius equation to determine the exciton binding energy (Eq. 1).

$$I(T) = I_0 / \left[1 + \mathrm{A} \cdot e^{-E_b/(k_B T)}\right] \quad (1)$$

where I_0 is the intensity at 0 K, E_b is the exciton binding energy, A is a proportional constant, and k_B is the Boltzmann constant (*52*). The calculated exciton binding energies of CP and MSP were 60.72 and 107.12 meV, respectively (Fig. 3C and Table 1). The increased exciton binding energy of MSP, which promotes radiative recombination through the spatial confinement of charge carriers, corresponds to the decreased grain size (~120 nm) of the MSP films (fig. S5) (*53*, *54*). The increased exciton binding energy in the MSP samples also implies that MSP is less susceptible to energy loss through nonradiative pathways (*51*). In particular, the MSP films exhibit prolonged average PL lifetimes (τ_{avg}) compared to the CP films, increasing significantly from 0.668 to 3.141 ns (Fig. 3D and Table 2). Furthermore, we examined the relationship between integrated PL (I_{PL}) and excitation pulse power (I_{ex}), specifically fluence, as described by the equation "$I_{PL} \propto (I_{ex})^k$". The exponent k reveals the degree of bimolecular recombination occurring. In particular, k values around 2 indicate the bimolecular recombination type recombination. As shown in fig. S6, the MSP films with a k value of 2.03 exhibit more pronounced bimolecular recombination compared to CP, which has a k value of 1.41. In addition, the PLQY

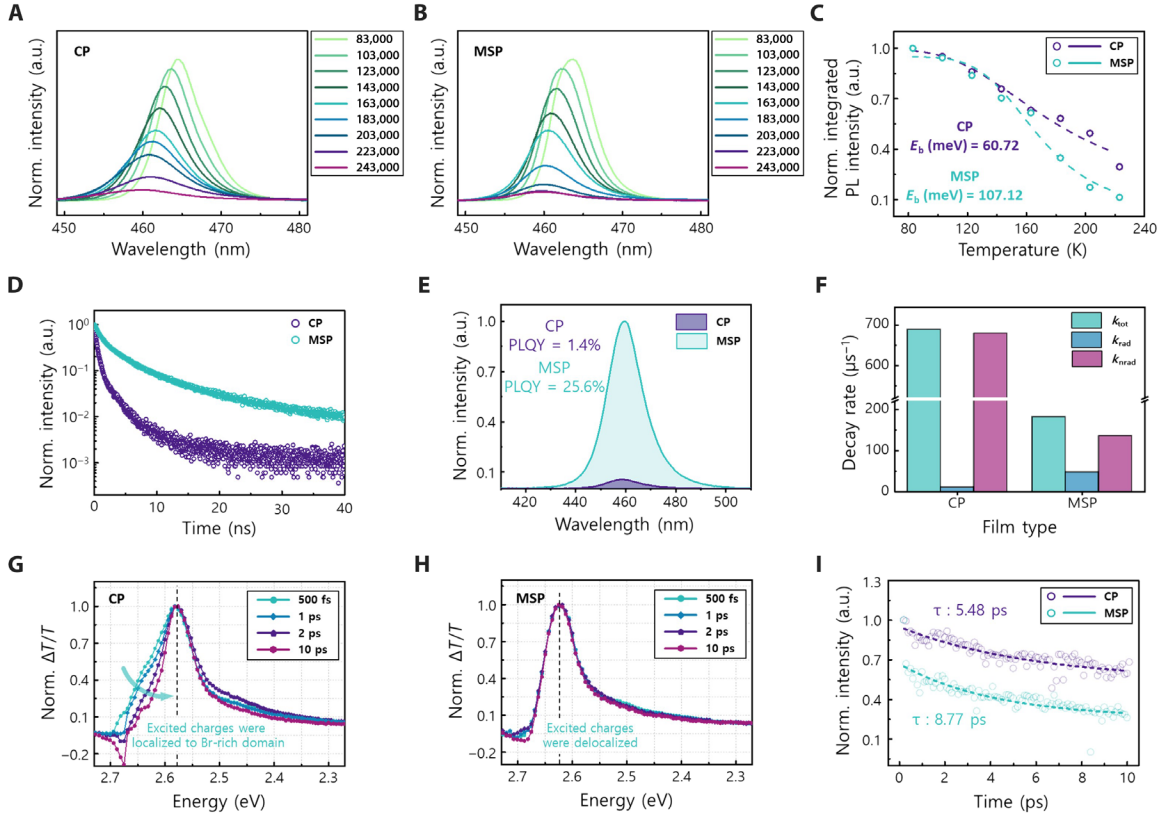

Fig. 3. Photophysical differences induced by sulfonate ligands. (**A** and **B**) Temperature-dependent PL spanning from 83 to 243 K in 20,000 steps for (A) CP and (B) MSP. (**C**) PL intensity [integrated from (A) and (B)] plotted as a function of temperature with a fitted line on the modified Arrhenius equation to derive the exciton binding energy. (**D**) Time-resolved PL decay curves for both CP and MSP, demonstrating lifetimes. (**E**) PL spectra for both CP and MSP, detailing the PLQY. (**F**) Total, radiative, and nonradiative decay rates for CP and MSP. (**G** and **H**) TAS spectra of (G) CP and (H) MSP across different time delays ranging from 500 fs to 10 ps. (**I**) TAS bleaching decay kinetics for CP at 2.57 eV and MSP at 2.62 eV.

Table 1. Exciton binding energy evaluation. Parameters were obtained from fitting the modified Arrhenius equation to the temperature-dependent PL data.

	A_0	E_b (meV)	R^2
CP	40.12	60.72	0.97
MSP	1575.25	107.12	0.98

Table 2. Exciton lifetime evaluation. Parameters were derived from fitting the biexponential decay equation to the time-resolved PL data.

	A_1	τ_1 (ns)	A_2	τ_2 (ns)	τ_{avg}	R^2
CP	0.96	0.511	0.045	4.00	0.69	0.99
MSP	0.66	1.159	0.34	6.90	3.14	0.99

increased from 1.38 to 25.6% without a peak shift (Fig. 3E and fig. S6). Compared to MSP, notably, ESP and PSP exhibited improved PLQY values at increased ligand concentrations, reaching 31.6 and 41.8%, respectively. The optimal PLQY values for MSP, ESP, and PSP were achieved at different ratios of ligands to lead ions: 0.6 for MS, 0.8 for ES, and 1.0 (or 1.2) for PS. The increased PLQY of the treated perovskite films implies that sulfonate ligands at the grain boundaries effectively passivate the defects. Furthermore, the radiative decay rate of CP was found to increase from 9.5 to 46.4 μs^{-1} in the MSP; simultaneously, the nonradiative recombination decay rate decreased from 678.9 to 134.9 μs^{-1} (Fig. 3F). These changes in the PL lifetime, PLQY, and decay rate are attributed to a reduction in trap sites, which are responsible for nonradiative recombination.

Furthermore, we used transient absorption spectroscopy (TAS) to investigate the impact of the sulfonate ligands on phase heterogeneity by observing variations in the bandwidth and spectral peak shift of the photobleaching band (Fig. 3, G and H) (*22*, *23*). In particular, the spectrum of CP reveals different energy states from 2.57 to 2.62 eV at 500 fs. However, after 10 ps, the spectra showed a noticeable decrease in intensity at 2.62 eV compared to that at 2.57 eV, resulting in an almost singular peak at 2.57 eV. This observation indicates the presence of heterogeneous phases within the CP film induced by the pump pulse energy. Notably, both CP and MSP exhibit the same PL peak locations (Fig. 3, A and B). In contrast, MSP demonstrates a single, narrow photobleaching band at 2.62 eV, indicating superior compositional homogeneity (*55*–*58*). In addition, we investigated the decay kinetics of the bleaching bands of CP at 2.57 eV and MSP at 2.62 eV to study the effect of the sulfonate ligand on relaxation dynamics (Fig. 3I). The time constants for CP and MSP were 5.48 and 8.77 ps, respectively. The faster decay time constant in CP is attributed to a higher density of defect sites that cause charge carrier trapping in CP compared to that in MSP (*59*). This can be explained by the compositional inhomogeneity or bandgap instability that stems from the nonuniform distribution of bromide and chloride ions. Therefore, sulfonate ligands have been proven to serve as effective passivating agents, thereby leading to prolonged relaxation times (*59*–*61*). This approach enabled us to gain insights into the structural robustness of perovskite materials and their capacity to preserve their integrity when subjected to various external stimuli.

High-brightness deep-blue PeLEDs using sulfonate ligands

As shown in Fig. 4A, we evaluated the impact of sulfonate ligands on device performance by fabricating deep-blue PeLEDs with a device structure of ITO/PEDOT:PSS:PFI:FS/perovskite/2,2′,2″-(1,3,5-benzinetriyl)-tris(1-phenyl-1-*H*-benzimidazole) (TPBi)/lithium fluoride (LiF)/Al. Given that we fabricated CP-, MSP-, ESP-, and PSP-based LEDs with a consistent ratio of cesium to lead ions, it can be deduced that any observed differences in performance and stability were not attributed to the introduction of additional cesium. Furthermore, an energy diagram of the device, derived from ultraviolet photoelectron spectroscopy, is shown in Fig. 4B and fig. S7 (*62*). The LED performance of the MSP notably surpassed that of the CP (Fig. 4, C and D), which was attributed to the effective elimination of trap-assisted nonradiative recombination achieved through the passivation of halide vacancies with MS ligands (*28*). Consequently, the EQE for MSP-based LEDs, with an emission peak at 461 nm and an FWHM of 15.4 nm, increases markedly to 3.05% from a considerably low EQE of 0.009% for CP-based LEDs. Of particular significance is the achievement of an L_{max} value of 2707 cd/m^2 for the MSP-based LEDs, which represents one of the brightest deep-blue PeLEDs reported to date satisfying Rec. 2020 standards (Fig. 4E) (*10*, *14*, *16*, *18*, *19*, *63*, *64*). Furthermore, ESP- and PSP-based LEDs were fabricated with various amount of ligands, achieving optimal PLQY for each ligand (fig. S6). Despite having rougher surfaces and slightly lower electron and hole mobilities (figs. S8 and S9), in comparison with MSP devices, both ESP and PSP showed a notable increase in PLQY at higher ligand concentrations. This PLQY enhancement allowed ESP- and PSP-based LEDs to achieve improved EQE of 3.96% and 5.68%, respectively (fig. S10). However, the decreased mobilities in ESP- and PSP-based LEDs resulted in decreased luminance of 2116 and 1978 cd/m^2, respectively. Furthermore, we have fabricated ESP- and PSP-based LED devices using the same ligand concentration as used in the MSP-based LED device. As shown in fig. S10, the EQE of ESP- and PSP-based LEDs was lower than that of MSP-based LEDs at the same ligand concentration, although three different films exhibited similar PLQY as shown in fig. S6. It can originate from the roughness differences, in which bigger roughness can induce trapping in the interface between perovskite film and the electron transporting layer. Furthermore, the decrease in L_{max} can stem from the increased dielectric property with a longer dielectric carbon chain.

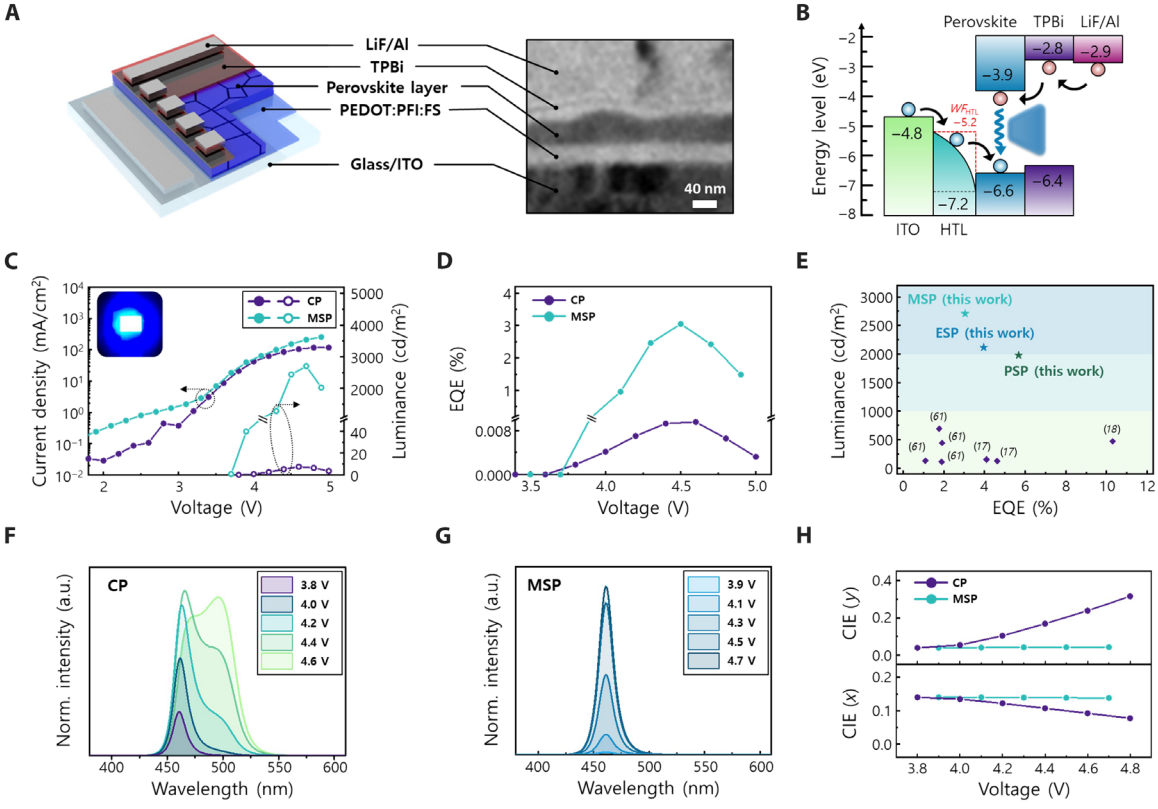

Fig. 4. Evaluation of device performances and color stability. (**A**) Schematic and transmission electron microscopy (TEM) image of the PeLED structure: glass/ITO/PEDOT:PSS:PFI:FS/perovskite/TPBi/LiF/Al. (**B**) Energy diagram of the PeLED devices; (**C**) Current-voltage (*I-V*) and luminance-voltage (*L-V*) curves for PeLEDs based on CP and MSP. (**D**) EQE-voltage (EQE-*V*) curves for PeLEDs based on CP and MSP. (**E**) Comparison of deep-blue PeLEDs satisfying Rec. 2020 standard below 465 nm of emission peak over the past 3 years. (**F** and **G**) Operating voltage-dependent electroluminescence (EL) spectra of PeLEDs based on (F) CP and (G) MSP. (**H**) Variations in CIE *x* and *y* coordinates under different operating voltages for PeLEDs constructed from CP and MSP.

We also investigated the influence of sulfonate ligands on color stability at different operating voltages. Figure 4F indicates the electroluminescence (EL) spectra obtained from CP-based LEDs, revealing color instability as the emission spectra shift when the operating voltage range varies between 3.8 and 5.0 V. In particular, a second emission peak at ~500 nm emerged and became dominant, notably overshadowing the original blue emission at ~460 nm. This phenomenon is attributed to the inherent structural instability of CP, which promotes the formation of Br-rich domains owing to ion migration through halide vacancies. Conversely, MSP-based LEDs demonstrate remarkably improved bandgap stability. The EL spectra of MSP-based LEDs exhibit a consistently maintained original blue peak, without any additional peaks, across the entire operating range from 3.9 to 4.7 V, as illustrated in Fig. 4G. These findings highlight the remarkable color stability of MSP-based LEDs compared to that of CP-based LEDs. In exploring the impact of ligand chain length on color purity, ESP and PSP LEDs showed slightly broader FWHM of 17.8 and 19.7 nm in their emission spectra, respectively. Furthermore, the main emission peaks of ESP- and PSP-based LEDs were red-shifted by ~2 nm from 461 to 463 nm (fig. S11). This relatively poor color stability compared to MSP-based LEDs could be attributed to their rougher surfaces. Notably, the perovskite grains in these LEDs did not form uniformly but appeared in sparse, pointed shapes with increasing the carbon chain length (fig. S8). These rougher surfaces could increase the grain boundaries, which are known sites for ion migration that can cause color instability (*65*). Despite these slight shifts in emission peaks for ESP- and PSP-based LEDs, their stability remains notably higher compared to CP-based LEDs (fig. S12). The spectral stability between CP- and MSP-based LEDs can be quantitatively compared using parameters such as the CIE coordinates, as depicted in Fig. 4H. For CP-based LEDs, the CIE *x* and *y* coordinates underwent significant shifts from 0.14 to 0.066 and 0.039 to 0.38, respectively. In contrast, the MSP-based LEDs displayed only minor changes in the CIE *x* and *y* coordinates, shifting from 0.14 to 0.138 and 0.039 to 0.042, respectively. Furthermore, extending the carbon chain length from MSP to PSP reduced the operational lifespan from 9.0 to 4.1 min when maintaining an initial luminance of 100 cd/m^2 (fig. S13). However, EL spectra of the three different samples showed negligible changes over time under a constant bias of ~3.95 V. This reduction may be attributed to enhanced joule heating facilitated by the longer dielectric carbon chains (*65*, *66*). In addition, the rougher surface morphologies associated with longer carbon chains potentially created more grain boundaries susceptible to ion migration, consequently leading to structural collapse (*65*, *66*). Furthermore, we conducted lifespan measurements of MSP-based LEDs under high-brightness conditions of 1000 cd/m^2 (fig. S14). The results revealed a significantly shorter lifespan of 1.35 min. This highlights the need for further research to enhance the longevity of PeLEDs under high-brightness conditions and facilitate their future commercialization.

DISCUSSION

In this study, we demonstrated that the incorporation of sulfonate ligands leads to highly luminous deep-blue PeLEDs with an L_{max} of 2707 cd/m^2, an EQE of 3.05%, and an emission peak at 461 nm with an FWHM of 15.4 nm. The maximum luminance achieved by MSP-based PeLEDs is among the highest recorded for deep-blue PeLEDs with an emission peak below 465 nm. Furthermore, we successfully enhanced the EQE of deep-blue PeLED to as high as 5.68% with a L_{max} of 1978 cd/m^2 at an emission peak of 461 nm by varying the chain length of the sulfonate ligands to construct PSP-based PeLEDs. Notably, these devices meet the Rec. 2020 standard and demonstrate one of the brightest luminescence outputs reported to date for deep-blue PeLEDs. Moreover, the devices maintained exceptional spectral stability, further highlighting the potential of the proposed molecular engineering strategy for enhancing the performance and stability of mixed-halide PeLEDs, which are particularly prone to phase segregation. We attribute the remarkable improvement in performance and spectral stability to sulfonate ligands, which effectively mitigate phase segregation and passivate the defects that foster nonradiative recombination. Therefore, our strategy holds promise for enhancing the performance of deep-blue PeLEDs to a level comparable to that of red and green PeLEDs, thereby facilitating the development of perovskite displays that comply with the Rec. 2020 standard.

MATERIALS AND METHODS

Materials

Lead(II) bromide ($PbBr_2$; 99.999%) and lead(II) chloride ($PbCl_2$; 99.999%), cesium bromide (CsBr; 99.999%), cesium MS, ethanesulfonic acid (95%), propanesulfonic acid (99%), dimethylsulfoxide (DMSO, 99.9%), Nafion PFI resin solution (tetrafluoroethylene-perfluoro-3,6-dioxa-4-methyl-7-octenesulfonic acid copolymer), isopropyl alcohol, FS, LiF (99.99%), and TPBi were purchased from Sigma-Aldrich Co. Ltd. In addition, the PEDOT:PSS aqueous solutions (Clevios AI4083) were purchased from Heraeus, Germany.

Preparation of perovskite precursor solution

Three specialized perovskite precursor solutions for fabrication of LEDs were meticulously prepared using specific compositions: For CP, $PbCl_2$, $PbBr_2$, and CsBr were mixed in a DMSO solvent at a concentration of 0.1 M with a stoichiometry of Cs:Pb:Br:Cl = 1.2:1:1.312:1.889. For MSP, $PbCl_2$, $PbBr_2$, cesium MS, and CsBr were combined in a DMSO solvent at a concentration of 0.1 M with a stoichiometry of Cs:Pb:Br:Cl:MS = 1.2:1:1.066:1.534:0.6. For ESP, $PbCl_2$, $PbBr_2$, cesium ES, and CsBr were blended in a DMSO solvent at a concentration of 0.1 M with a stoichiometry of Cs:Pb:Br:Cl:ES = 1.2:1:0.982:1.418:0.8. For PSP, $PbCl_2$, $PbBr_2$, cesium PS, and CsBr were dissolved in a DMSO solvent at a concentration of 0.1 M with a stoichiometry of Cs:Pb:Br:Cl:PS = 1.2:1:0.9:1.3:1.0. For each solution, the Cl/Br ratio was consistently maintained at 1.44.

Fabrication of PeLEDs

LEDs were produced on ITO-coated glass substrates with a thickness of 0.70 ± 0.005 mm. The ITO layer had a thickness of 900 ± 25 Å. The substrates underwent a rigorous cleaning process involving acetone and isopropanol in an ultrasonic washer, followed by treatment with oxygen plasma for 10 min. A solution comprising PEDOT:PSS, PFI, FS, and isopropyl alcohol in a volume ratio of 10:3:3:10 was spin-coated at 9000 rpm for 50 s. This was followed by annealing on a hotplate at 150°C for 60 min. After cooling to room temperature, a perovskite precursor solution (0.1 M) was spin-coated onto the PEDOT:PSS:PFI:FS layer at 2500 rpm for 60 s, with chloroform antisolvent treatment and a 20-min bake at 150°C. Subsequently, the substrates were transferred to a high-vacuum thermal evaporator. Using a shadow mask, sequential layers of TPBi (~25 nm), LiF (~1 nm), and Al (~100 nm) were deposited at pressures below 10^{-7} torr.

Synthesis of cesium sulfonate salts

Sulfonate salts can be synthesized from sulfonic acids via a simple acid-base reaction. CsOH dissolved in 1 ml of water was added to sulfonic acid in an ice bath. The mixture was stirred for ~1 hour until a solid powder formed. Last, it was treated with acetone to remove any remaining acid and dried in a vacuum oven.

Characterization

The chemical bonds in the samples were analyzed by XPS using a Thermo VG Scientific K-alpha instrument. The cross sections of the devices were analyzed by transmission electron microscopy (TEM) using a JEOL JEM-ARM200F instrument. The vibrational modes of the samples were examined by FTIR spectroscopy using a Nicolet iS50 FTIR spectrometer. The PL characteristics of the samples were investigated using a PL spectrometer (LabRAM HR Evolution Visible NIR, HORIBA). The crystal structure of the samples was determined by XRD using a RIGAKU D/MAX 2500 instrument. The EL spectra and current-voltage-luminance characteristics of the devices were measured using a spectroradiometer (CS-2000, Konika Minolta) and programmable source meter (Keithley model 2400), respectively, to investigate their optical and electrical properties.

Femtosecond TAS

Transient absorption spectroscopy (TAS) spectra were recorded for CP and MSP with smaller bandgaps compared to those used for device fabrication because of the constraints of the excitation energy range using femtosecond laser pulses based on a visible pump-continuum probe scheme. Output pulses of 1.55 eV from a Ti:sapphire-amplified laser (Coherent Legend Elite) were split into the pump and probe arms. On the pump arm, laser pulses of 1.55 eV were converted into pump pulses of 2.63 eV. On the probe arm, the laser pulses of 1.55 eV were directed into a c-cut sapphire window with a thickness of 3 mm and converted into a white-light continuum spanning from 2.76 to 1.72 eV by self-phase modulation. The generated white-light continuum was used as the supercontinuum probe pulse without further compensation of the dispersion. The probe pulses were time-delayed with respect to the pump pulses using a motorized translation stage (Newport, M-ILS150HA). The transient absorption signal spectra were recorded using a spectrometer (Andor SR303i) equipped with a Si charge-coupled device (Andor, DU420A). In all the measurements, the polarization of the pump pulses was set at a magic angle (54.7°) relative to that of the probe pulses to eliminate any anisotropic signals. The estimated time resolution of the transient absorption measurement was less than 80 fs, as determined by the optical heterodyne-detected optical Kerr effect measurement of a pure solvent (CCl_4) at the sample position. The perovskite films were placed at the sample position, and their optical densities were adjusted to a range of 0.2 to 0.3 at the excitation wavelength. The transient absorption spectra of the perovskites were collected over a time range of up to 850 ps.

Supplementary Materials

This PDF file includes:

Figs. S1 to S14
Table S1

REFERENCES AND NOTES

1. Y. Hassan, J. H. Park, M. L. Crawford, A. Sadhanala, J. Lee, J. C. Sadighian, E. Mosconi, R. Shivanna, E. Radicchi, M. Jeong, C. Yang, H. Choi, S. H. Park, M. H. Song, F. De Angelis, C. Y. Wong, R. H. Friend, B. R. Lee, H. J. Snaith, Ligand-engineered bandgap stability in mixed-halide perovskite LEDs. *Nature* **591**, 72–77 (2021).
2. A. Liu, H. Zhu, S. Bai, Y. Reo, T. Zou, M.-G. Kim, Y.-Y. Noh, High-performance inorganic metal halide perovskite transistors. *Nat. Electron.* **5**, 78–83 (2022).
3. H. Min, D. Y. Lee, J. Kim, G. Kim, K. S. Lee, J. Kim, M. J. Paik, Y. K. Kim, K. S. Kim, M. G. Kim, T. J. Shin, S. Il Seok, Perovskite solar cells with atomically coherent interlayers on SnO_2 electrodes. *Nature* **598**, 444–450 (2021).
4. G. Pacchioni, Highly efficient perovskite LEDs. *Nat. Rev. Mater.* **6**, 108–108 (2021).
5. J. Kim, K.-W. Seo, S. Lee, K. Kim, C. Kim, J.-Y. Lee, All-in-one process for color tuning and patterning of perovskite quantum dot light-emitting diodes. *Adv. Sci.* **9**, 2200073 (2022).
6. Y. Shang, Y. Liao, Q. Wei, Z. Wang, B. Xiang, Y. Ke, W. Liu, Z. Ning, Highly stable hybrid perovskite light-emitting diodes based on Dion-Jacobson structure. *Sci. Adv.* **5**, eaaw8072 (2019).
7. L. N. Quan, B. P. Rand, R. H. Friend, S. G. Mhaisalkar, T.-W. Lee, E. H. Sargent, Perovskites for next-generation optical sources. *Chem. Rev.* **119**, 7444–7477 (2019).
8. Y.-H. Kim, S. Kim, A. Kakekhani, J. Park, J. Park, Y.-H. Lee, H. Xu, S. Nagane, R. B. Wexler, D.-H. Kim, S. H. Jo, L. Martínez-Sarti, P. Tan, A. Sadhanala, G.-S. Park, Y.-W. Kim, B. Hu, H. J. Bolink, S. Yoo, R. H. Friend, A. M. Rappe, T.-W. Lee, Comprehensive defect suppression in perovskite nanocrystals for high-efficiency light-emitting diodes. *Nat. Photon.* **15**, 148–155 (2021).
9. Y.-K. Wang, F. Yuan, Y. Dong, J.-Y. Li, A. Johnston, B. Chen, M. I. Saidaminov, C. Zhou, X. Zheng, Y. Hou, K. Bertens, H. Ebe, D. Ma, Z. Deng, S. Yuan, R. Chen, L. K. Sagar, J. Liu, J. Fan, P. Li, X. Li, Y. Gao, M.-K. Fung, Z.-H. Lu, O. M. Bakr, L.-S. Liao, E. H. Sargent, All-inorganic quantum-dot LEDs BASED on a phase-stabilized α-$CsPbI_3$ perovskite. *Angew. Chem. Int. Ed.* **60**, 16164–16170 (2021).
10. G. Zou, Z. Li, Z. Chen, L. Chu, H.-L. Yip, Y. Cao, Color-stable deep-blue perovskite light-emitting diodes based on organotrichlorosilane post-treatment. *Adv. Funct. Mater.* **31**, 2103219 (2021).
11. X. Yang, X. Zhang, J. Deng, Z. Chu, Q. Jiang, J. Meng, P. Wang, L. Zhang, Z. Yin, J. You, Efficient green light-emitting diodes based on quasi-two-dimensional composition and phase engineered perovskite with surface passivation. *Nat. Commun.* **9**, 570 (2018).
12. M. Zhang, C. Zuo, J. Tian, L. Ding, Blue perovskite LEDs. *J. Semicon.* **42**, 070201 (2021).
13. Y. Tian, C. Zhou, M. Worku, X. Wang, Y. Ling, H. Gao, Y. Zhou, Y. Miao, J. Guan, B. Ma, Highly efficient spectrally stable red perovskite light-emitting diodes. *Adv. Mater.* **30**, 1707093 (2018).
14. Y. Jiang, C. Sun, J. Xu, S. Li, M. Cui, X. Fu, Y. Liu, Y. Liu, H. Wan, K. Wei, T. Zhou, W. Zhang, Y. Yang, J. Yang, C. Qin, S. Gao, J. Pan, Y. Liu, S. Hoogland, E. H. Sargent, J. Chen, M. Yuan, Synthesis-on-substrate of quantum dot solids. *Nature* **612**, 679–684 (2022).
15. Y. Nah, D. Solanki, Y. Dong, J. A. Röhr, A. D. Taylor, S. Hu, E. H. Sargent, D. H. Kim, Narrowing the phase distribution of quasi-2D perovskites for stable deep-blue electroluminescence. *Adv. Sci.* **9**, 2201807 (2022).
16. H. Liu, M. Worku, A. Mondal, T. B. Shonde, M. Chaaban, A. Ben-Akacha, S. Lee, F. Gonzalez, O. Olasupo, X. Lin, J. S. R. Vellore Winfred, Y. Xin, E. Lochner, B. Ma, Efficient and stable blue light emitting diodes based on $CsPbBr_3$ nanoplatelets with surface passivation by a multifunctional organic sulfate. *Adv. Energy Mater.* **13**, 2201605 (2023).
17. Z. Liu, W. Qiu, X. Peng, G. Sun, X. Liu, D. Liu, Z. Li, F. He, C. Shen, Q. Gu, F. Ma, H.-L. Yip, L. Hou, Z. Qi, S.-J. Su, Perovskite light-emitting diodes with EQE exceeding 28% through a synergetic dual-additive strategy for defect passivation and nanostructure regulation. *Adv. Mater.* **33**, 2103268 (2021).
18. S. Yuan, L.-S. Cui, L. Dai, Y. Liu, Q.-W. Liu, Y.-Q. Sun, F. Auras, M. Anaya, X. Zheng, E. Ruggeri, Y.-J. Yu, Y.-K. Qu, M. Abdi-Jalebi, O. M. Bakr, Z.-K. Wang, S. D. Stranks, N. C. Greenham, L.-S. Liao, R. H. Friend, Efficient and spectrally stable blue perovskite light-emitting diodes employing a cationic π-conjugated polymer. *Adv. Mater.* **33**, 2103640 (2021).
19. J. Dong, F. Lu, D. Han, J. Wang, Z. Zang, L. Kong, Y. Zhang, X. Ma, J. Zhou, H. Ji, X. Yang, N. Wang, Deep-blue electroluminescence of perovskites with reduced dimensionality achieved by manipulating adsorption-energy differences. *Angew. Chem. Int. Ed.* **61**, e202210322 (2022).
20. J. Jiang, Z. Chu, Z. Yin, J. Li, Y. Yang, J. Chen, J. Wu, J. You, X. Zhang, Red perovskite light-emitting diodes with efficiency exceeding 25% realized by co-spacer cations. *Adv. Mater.* **34**, 2204460 (2022).
21. J. S. Kim, J.-M. Heo, G.-S. Park, S.-J. Woo, C. Cho, H. J. Yun, D.-H. Kim, J. Park, S.-C. Lee, S.-H. Park, E. Yoon, N. C. Greenham, T.-W. Lee, Ultra-bright, efficient and stable perovskite light-emitting diodes. *Nature* **611**, 688–694 (2022).
22. Y.-H. Zhou, C. Wang, S. Yuan, C. Zou, Z. Su, K.-L. Wang, Y. Xia, B. Wang, D. Di, Z.-K. Wang, L.-S. Liao, Stabilized low-dimensional species for deep-blue perovskite light-emitting diodes with EQE approaching 3.4%. *J. Am. Chem. Soc.* **144**, 18470–18478 (2022).
23. Y. Liu, L. K. Ono, G. Tong, T. Bu, H. Zhang, C. Ding, W. Zhang, Y. Qi, Spectral stable blue-light-emitting diodes via asymmetric organic diamine based Dion–Jacobson perovskites. *J. Am. Chem. Soc.* **143**, 19711–19718 (2021).
24. Y. Jiang, J. Wei, M. Yuan, Energy-funneling process in quasi-2D perovskite light-emitting diodes. *J. Phys. Chem. Lett.* **12**, 2593–2606 (2021).
25. D. P. Nenon, K. Pressler, J. Kang, B. A. Koscher, J. H. Olshansky, W. T. Osowiecki, M. A. Koc, L.-W. Wang, A. P. Alivisatos, Design principles for trap-free $CsPbX_3$ nanocrystals: Enumerating and eliminating surface halide vacancies with softer Lewis bases. *J. Am. Chem. Soc.* **140**, 17760–17772 (2018).
26. X. Zheng, S. Yuan, J. Liu, J. Yin, F. Yuan, W.-S. Shen, K. Yao, M. Wei, C. Zhou, K. Song, B.-B. Zhang, Y. Lin, M. N. Hedhili, N. Wehbe, Y. Han, H.-T. Sun, Z.-H. Lu, T. D. Anthopoulos, O. F. Mohammed, E. H. Sargent, L.-S. Liao, O. M. Bakr, Chlorine vacancy passivation in mixed halide perovskite quantum dots by organic pseudohalides enables efficient Rec. 2020 blue light-emitting diodes. *ACS Energy Lett.* **5**, 793–798 (2020).
27. Z. Li, K. Cao, J. Li, Y. Tang, X. Ding, B. Yu, Review of blue perovskite light emitting diodes with optimization strategies for perovskite film and device structure. *Opto-Electron. Adv.* **4**, 200019 (2021).
28. C. Bi, Z. Yao, X. Sun, X. Wei, J. Wang, J. Tian, Perovskite quantum dots with ultralow trap density by acid etching-driven ligand exchange for high luminance and stable pure-blue light-emitting diodes. *Adv. Mater.* **33**, 2006722 (2021).
29. M. C. Brennan, S. Draguta, P. V. Kamat, M. Kuno, Light-induced anion phase segregation in mixed halide perovskites. *ACS Energy Lett.* **3**, 204–213 (2018).
30. S. G. Motti, J. B. Patel, R. D. J. Oliver, H. J. Snaith, M. B. Johnston, L. M. Herz, Phase segregation in mixed-halide perovskites affects charge-carrier dynamics while preserving mobility. *Nat. Commun.* **12**, 6955 (2021).
31. K. Wang, Z. Gao, W. Zhang, Y. Yan, H. Song, X. Lin, Z. Zhou, H. Meng, A. Xia, J. Yao, Y. S. Zhao, Exciton funneling in light-harvesting organic semiconductor microcrystals for wavelength-tunable lasers. *Sci. Adv.* **5**, eaaw2953 (2019).
32. X. Wang, L. Cai, Y. Zou, D. Liang, L. Wang, Y. Li, J. Zang, G. Bai, X. Gao, T. Song, B. Sun, Unveiling the critical role of ammonium bromide in blue emissive perovskite films. *Nanoscale* **13**, 13497–13505 (2021).
33. F. Ye, H. Yan, S. Liu, B. Liu, Z. Zhang, M. Tian, T. Zheng, X. Lan, J. Huang, C. Meng, P. Xu, G. Li, Interface engineering with quaternary ammonium-based ionic liquids toward efficient blue perovskite light-emitting diodes. *ACS Appl. Mater. Interfaces* **14**, 50393–50400 (2022).
34. C. B. Park, Y. S. Shin, Y. J. Yoon, H. Jang, J. G. Son, S. Kim, N. G. An, J. W. Kim, Y. C. Jun, G.-H. Kim, J. Y. Kim, Suppression of halide migration and immobile ionic surface passivation for blue perovskite light-emitting diodes. *J. Mater. Chem. C* **10**, 2060–2066 (2022).
35. X. Zou, L.-H. Huo, Z.-P. Deng, H. Zhao, S. Gao, Structure extension in two Pb(II)–sulfonate complexes from hemidirected to holodirected Pb(II) by secondary Pb–O interactions. *Inorg. Chem. Commun.* **46**, 305–309 (2014).
36. P. M. Shanthi, P. J. Hanumantha, K. Ramalinga, B. Gattu, M. K. Datta, P. N. Kumta, Sulfonic acid based complex framework materials (CFM): Nanostructured polysulfide immobilization systems for rechargeable lithium–sulfur battery. *J. Electrochem. Soc.* **166**, A1827–A1835 (2019).
37. H. Cho, S.-H. Jeong, M.-H. Park, Y.-H. Kim, C. Wolf, C.-L. Lee, J. H. Heo, A. Sadhanala, N. Myoung, S. Yoo, S. H. Im, R. H. Friend, T.-W. Lee, Overcoming the electroluminescence efficiency limitations of perovskite light-emitting diodes. *Science* **350**, 1222–1225 (2015).
38. B. Li, J. Zhen, Y. Wan, X. Lei, Q. Liu, Y. Liu, L. Jia, X. Wu, H. Zeng, W. Zhang, Anchoring fullerene onto perovskite film via grafting pyridine toward enhanced electron transport in high-efficiency solar cells. *ACS Appl. Mater. Interfaces* **10**, 32471–32482 (2018).
39. Z. Wu, M. Jiang, Z. Liu, A. Jamshaid, L. K. Ono, Y. Qi, Highly efficient perovskite solar cells enabled by multiple ligand passivation. *Adv. Energy Mater.* **10**, 1903696 (2020).
40. J. He, J. Liu, Y. Hou, Y. Wang, S. Yang, H. G. Yang, Surface chelation of cesium halide perovskite by dithiocarbamate for efficient and stable solar cells. *Nat. Commun.* **11**, 4237 (2020).
41. Z. Yan-Min, Study on naphthalene sulfonic acid formaldehyde condensate by ultraviolet absorption spectrum. *J. Phys. Conf. Ser.* **1237**, 022107 (2019).
42. A. Garai, R. K. Behera, N. Pradhan, Facet chemistry and the impact of surface ligands on the photoluminescence of different polyhedral-shaped $CsPbBr_3$ perovskite nanocrystals. *J. Phys. Chem. C* **126**, 16759–16766 (2022).
43. M.-H. Jao, C.-F. Lu, P.-Y. Tai, W.-F. Su, Precise facet engineering of perovskite single crystals by ligand-mediated strategy. *Cryst. Growth Des.* **17**, 5945–5952 (2017).
44. C.-H. Kuan, S.-H. Yang, Surface ligand engineering of perovskite nanocrystals with a conjugated sulfonate ligand for light-emitting applications. *Mater. Adv.* **3**, 7824–7832 (2022).

45. C. Ma, M.-C. Kang, S.-H. Lee, S. J. Kwon, H.-W. Cha, C.-W. Yang, N.-G. Park, Photovoltaically top-performing perovskite crystal facets. *Joule* **6**, 2626–2643 (2022).
46. M. Liao, B.-B. Yu, Z. Jin, W. Chen, Y. Zhu, X. Zhang, W. Yao, T. Duan, I. Djerdj, Z. He, Efficient and stable $FASnI_3$ perovskite solar cells with effective interface modulation by low-dimensional perovskite layer. *ChemSusChem* **12**, 5007–5014 (2019).
47. Z. Ren, J. Sun, J. Yu, X. Xiao, Z. Wang, R. Zhang, K. Wang, R. Chen, Y. Chen, W. C. H. Choy, High-performance blue quasi-2D perovskite light-emitting diodes via balanced carrier confinement and transfer. *Nano-Micro Lett.* **14**, 66 (2022).
48. J. Ma, L. Yang, Y. Zhang, Y. Kuang, M. Shao, Rearranging the phase distribution of quasi-2D perovskite for efficient and narrow emission perovskite light-emitting diodes. *J. Phys. Chem. Lett.* **13**, 4739–4746 (2022).
49. H. Zhao, H. Chen, S. Bai, C. Kuang, X. Luo, P. Teng, C. Yin, P. Zeng, L. Hou, Y. Yang, L. Duan, F. Gao, M. Liu, High-brightness perovskite light-emitting diodes based on $FAPbBr_3$ nanocrystals with rationally designed aromatic ligands. *ACS Energy Lett.* **6**, 2395–2403 (2021).
50. H. Wang, X. Zhang, Q. Wu, F. Cao, D. Yang, Y. Shang, Z. Ning, W. Zhang, W. Zheng, Y. Yan, S. V. Kershaw, L. Zhang, A. L. Rogach, X. Yang, Trifluoroacetate induced small-grained $CsPbBr_3$ perovskite films result in efficient and stable light-emitting devices. *Nat. Commun.* **10**, 665 (2019).
51. H. Zhang, F. Ye, W. Li, R. S. Gurney, D. Liu, C. Xiong, T. Wang, Improved performance of perovskite light-emitting diodes by dual passivation with an ionic additive. *ACS Appl. Energy Mater.* **2**, 3336–3342 (2019).
52. C. Li, J. Liu, H. Li, K. Wu, J. Wang, Q. Yang, Covalent organic frameworks with high quantum efficiency in sacrificial photocatalytic hydrogen evolution. *Nat. Commun.* **13**, 2357 (2022).
53. J.-M. Heo, H. Cho, S.-C. Lee, M.-H. Park, J. S. Kim, H. Kim, J. Park, Y.-H. Kim, H. J. Yun, E. Yoon, D.-H. Kim, S. Ahn, S.-J. Kwon, C.-Y. Park, T.-W. Lee, Bright lead-free inorganic $CsSnBr_3$ perovskite light-emitting diodes. *ACS Energy Lett.* **7**, 2807–2815 (2022).
54. H. Cho, J. S. Kim, C. Wolf, Y.-H. Kim, H. J. Yun, S.-H. Jeong, A. Sadhanala, V. Venugopalan, J. W. Choi, C.-L. Lee, R. H. Friend, T.-W. Lee, High-efficiency polycrystalline perovskite light-emitting diodes based on mixed cations. *ACS Nano* **12**, 2883–2892 (2018).
55. T. He, S. Li, Y. Jiang, C. Qin, M. Cui, L. Qiao, H. Xu, J. Yang, R. Long, H. Wang, M. Yuan, Reduced-dimensional perovskite photovoltaics with homogeneous energy landscape. *Nat. Commun.* **11**, 1672 (2020).
56. M. Karlsson, Z. Yi, S. Reichert, X. Luo, W. Lin, Z. Zhang, C. Bao, R. Zhang, S. Bai, G. Zheng, P. Teng, L. Duan, Y. Lu, K. Zheng, T. Pullerits, C. Deibel, W. Xu, R. Friend, F. Gao, Mixed halide perovskites for spectrally stable and high-efficiency blue light-emitting diodes. *Nat. Commun.* **12**, 361 (2021).
57. F. Brivio, C. Caetano, A. Walsh, Thermodynamic origin of photoinstability in the $CH_3NH_3Pb(I_{1-x}Br_x)_3$ hybrid halide perovskite alloy. *J. Phys. Chem. Lett.* **7**, 1083–1087 (2016).
58. X. Wang, Y. Ling, X. Lian, Y. Xin, K. B. Dhungana, F. Perez-Orive, J. Knox, Z. Chen, Y. Zhou, D. Beery, Suppressed phase separation of mixed-halide perovskites confined in endotaxial matrices. *Nat. Commun.* **10**, 625 (2019).
59. L. Wang, C. McCleese, A. Kovalsky, Y. Zhao, C. Burda, Femtosecond time-resolved transient absorption spectroscopy of $CH_3NH_3PbI_3$ perovskite films: Evidence for passivation effect of PbI_2. *J. Am. Chem. Soc.* **136**, 12205–12208 (2014).
60. T. Supasai, N. Rujisamphan, K. Ullrich, A. Chemseddine, T. Dittrich, Formation of a passivating $CH_3NH_3PbI_3/PbI_2$ interface during moderate heating of $CH_3NH_3PbI_3$ layers. *Appl. Phys. Lett.* **103**, (2013).
61. K. Wang, Z.-Y. Lin, Z. Zhang, L. Jin, K. Ma, A. H. Coffey, H. R. Atapattu, Y. Gao, J. Y. Park, Z. Wei, B. P. Finkenauer, C. Zhu, X. Meng, S. N. Chowdhury, Z. Chen, T. Terlier, T.-H. Do, Y. Yao, K. R. Graham, A. Boltasseva, T.-F. Guo, L. Huang, H. Gao, B. M. Savoie, L. Dou, Suppressing phase disproportionation in quasi-2D perovskite light-emitting diodes. *Nat. Commun.* **14**, 397 (2023).
62. K.-G. Lim, S. Ahn, Y.-H. Kim, Y. Qi, T.-W. Lee, Universal energy level tailoring of self-organized hole extraction layers in organic solar cells and organic–inorganic hybrid perovskite solar cells. *Energ. Environ. Sci.* **9**, 932–939 (2016).
63. Y. C. Kim, H. J. An, D. H. Kim, J.-M. Myoung, Y. J. Heo, J. H. Cho, High-performance perovskite-based blue light-emitting diodes with operational stability by using organic ammonium cations as passivating agents. *Adv. Funct. Mater.* **31**, 2005553 (2021).
64. Y. Jia, R. Li, Y. Zhou, S. Zhao, H. Yu, J. Wang, Z. Lin, H. Su, N. Zhao, Unveiling the complex evolution in mixed Br–Cl perovskite precursors for high-efficiency deep-blue light-emitting diodes. *Small Structures* **4**, 2200393 (2023).
65. Y. Shao, Y. Fang, T. Li, Q. Wang, Q. Dong, Y. Deng, Y. Yuan, H. Wei, M. Wang, A. Gruverman, J. Shield, J. Huang, Grain boundary dominated ion migration in polycrystalline organic–inorganic halide perovskite films. *Energ. Environ. Sci.* **9**, 1752–1759 (2016).
66. Y. Zou, T. Wu, F. Fu, S. Bai, L. Cai, Z. Yuan, Y. Li, R. Li, W. Xu, T. Song, Y. Yang, X. Gao, F. Gao, B. Sun, Thermal-induced interface degradation in perovskite light-emitting diodes. *J. Mater. Chem. C* **8**, 15079–15085 (2020).

Acknowledgments

Funding: We sincerely appreciate the financial support from the Basic Science Research Program through the National Research Foundation of Korea (NRF) funded by the Korea government (MSIT) (no. 2023R1A2C3003245) and Institute for Basic Science (IBS-R033).

Author contributions: J.-Y.L. supervised the project and provided guidance throughout the study. Seungjae Lee, J.K., and J.L. jointly conceived and designed the experiments and prepared the manuscript. Seungjae Lee and J.K. fabricated the LED devices. Seungjae Lee, J.K., H.K., Changwon Kim, S.K., Changjo Kim, H.L., C.M., T.K., J.L., Seungbok Lee, and B.C. performed various analyses including FTIR, XRD, XPS, TEM, and TAS to investigate the physical and chemical properties of the samples. All the authors discussed the results and provided critical feedback on the manuscript. **Competing interests:** The authors declare that they have no competing interests. **Data and materials availability:** All data needed to evaluate the conclusions in the paper are present in the paper and/or the Supplementary Materials.

Submitted 3 January 2024
Accepted 15 April 2024
Published 17 May 2024
10.1126/sciadv.adn8465